Supporting Information

Manipulating the Interfacial Energetics of n-type Silicon Photoanode for Efficient Water Oxidation

Tingting Yao,[†,‡] Ruotian Chen,[†,‡,∥] Junjie Li,[⊥] Jingfeng Han,[†,‡,§] Wei Qin,[†,‡] Hong Wang,[†,‡,∥] Jingying Shi,[†,‡] Fengtao Fan,[†,‡,§] and Can Li*[,†,‡,§]

[†]State Key Laboratory of Catalysis, [‡]Dalian National Laboratory for Clean Energy, [§]The Collaborative Innovation Center of Chemistry for Energy Materials (iChEM), Dalian Institute of Chemical Physics, Chinese Academy of Sciences, Zhongshan Road 457, Dalian, 116023, China

[∥]University of Chinese Academy of Sciences, Beijing, 100049, China

[⊥]International Iberian Nanotechnology Laboratory (INL), Avenida Mestre Jose Veiga, Braga 4715-330, Portugal

This PDF file includes:

Experimental Section

Silicon wafers

Polished n-type Si (100) wafers (0.1-1 Ω cm, 400 μm thickness) were purchased from China Electronics Technology Group Corporation No. 46 Research Institute. The Si wafers were ultrasonically cleaned in acetone, isopropanol, ethanol (Sinopharm Chemical Regent Co. Ltd, AR) and deionized water (>18.2 MΩ cm^{-1}) for 20min, respectively. Before all usage, the silicon wafers were dipped in a 10% HF solution for 10 s to remove the surface oxide layer, and washed with deionized water. Then the wafers were transferred into the reaction chamber immediately. A 200 nm Al film was evaporated on the back side of the silicon followed with an annealing process to form an ohmic contact.

Atom layered deposition (ALD) of TiO_x

TiO_x was deposited at 150℃ with tetrakisdimethylamido titanium (TDMAT) as the titanium source (80 ℃) and H_2O as the oxidant (room temperature) through ALD method. In a typical process, the TDMAT was pulse with 0.03 s, and a pulse time with 0.04 s for the H_2O. The thickness of the TiO_x film was controlled by the number of cycles.

Magnetron sputtering deposition of ITO

ITO deposition was performed by R. F. reactive magnetron sputtering system (Kurt J. Lesker Company PVD 75) with an ITO target. The sputtering target is In_2O_3: SnO_2 (90%: 10%) with a purity of 99.95%. The target-substrate spacing was kept at 170 mm. Before deposition, the chamber was evacuated to 10^{-7} Torr, and then high purity Ar was introduced into the chamber. The gas flows were controlled by individual mass flow controllers. All depositions were conducted at 2 mTorr. The sputtering power was 50 W. No extra heating and biasing were applied for the substrate during or post deposition. The deposition time is regulated to achieve films with different thickness. 50 nm ITO layer was used for the solid-state cells measurement, and 10 nm ITO layer was used for photoelectrodes tested in solution. The samples were heated to 450℃ for 30 min in a forming gas environment (95% Ar, 5% H_2).

Photoelectrochemical deposition of NiOOH

In order to prepare n-Si/TiO_x/ITO/NiOOH photoanode, 0.1 M $NiSO_4$ solution with pH value adjusted to 6.65~6.7 by carefully adding NaOH was prepared. The solution were purged with Ar gas for at least 30 min before deposition. During illumination, the photogenerated holes in

n-Si/TiO_x/ITO device oxidized Ni^{2+} to Ni^{3+} ions, and Ni^{3+} ions were precipitated as NiOOH. The deposition processes were carried out under galvanostatic method with a current density of 10 uA cm^{-2} for 2200s.[1]

Photoelectrochemical (PEC) measurement

All photoelectrochemical and electrochemical measurements were performed in electrolyte solutions prepared with deionized pure water (>18.2 MΩ▪cm^{-1}). The ferri/ferrocyanide solution was made to be 5 mM of both $K_3Fe(CN)_6$ and $K_4Fe(CN)_6$▪$3H_2O$ in 1 M aqueous KCl. The electrolyte for photoelectrochemical or electrochemical water oxidation was 1 M LiOH aqueous solution (pH 12). A Pt foil was used as a counter electrode, and the SCE was used as a reference electrode. The cyclic voltammetry curves were measured at 100 mV S^{-1}. Potentials measured versus SCE were converted to RHE, $V_{RHE} = V_{SCE} + 0.242 + 0.059 * pH$. All measurements were conducted in air at room temperature. Illumination was provided by an AM 1.5G solar simulator, and the intensity was adjusted to 1 sun by means of a calibrated photodiode.

The Schottky capacitor fabrication and capacitance analysis

For solid-state cells measurements, the ITO layer with 50 nm thickness was deposited on the n-Si or n-Si/TiO_x surface through a shadow mask defining a diameter of 0.6 cm for circular capacitors. Two gold needles contacted with the Al back contact and ITO gate layer, separately. Measurements were carried out on a PARSTAT 2273 workstation (Princeton Applied Research) at room temperature. Scans were taken sweeping from depletion to accumulation with a superimposed 10 mV AC voltage to measure the capacitance between 100 Hz and 100 KHz.

The KPFM and SPV characteristics

The n-Si/ITO and n-Si/30C-TiO_x/ITO photoanodes with 10 nm ITO layer was used for Kelvin Probe Force Microscopy (KPFM) and surface photovoltage (SPV) analysis. A commercial Bruker AFM with the AM-KPFM imaging mode in air was used, and the KPFM was carried out in Lift mode. The surface potentials of the device with different coating layers in the dark state were examined by KPFM.[2] Moreover, the corresponding SPV which reflect the built-in electrical field were acquired with correlated KPFM and transient SPV techniques.[3,4] The measured contact potential difference (CPD) in KPFM can be calculated as $\mathrm{CPD} = (\Phi_{tip} - \Phi_{sample})/-e$, where Φ_{tip} and Φ_{sample} are the work functions of the kelvin tip and the sample surface, and e is the electronic charge.[2] The SPV is defined as the changes of surface potential before and after

illumination which can be calculated as $\mathrm{SPV} = \Delta\mathrm{CPD} = CPD_{light} - CPD_{dark}$, where CPD_{light} and CPD_{dark} are the CPD measured in dark and light.[3] The relative magnitudes of SPV can be obtained by lock-in amplifier with chopped light. In such a manner, we can get more clear and comparable strength of built-in electrical fields. In this case, the $\mathrm{SPV} = k^{*}|\Delta CPD|$, where k is a constant of lock-in amplifier, and $|\Delta CPD|$ is the absolute value of actual SPV. In such a manner, we can get more clear and comparable strength of built-in electrical fields.

XPS and UV-Vis-NIR characteristics

The TiO_x films with different thickness were deposited on the surface of n-Si and annealed before X-ray photoelectron spectroscopy (XPS) testing. Coating TiO_x with ITO layer will eliminate the XPS peak of Ti 2p. The XPS measurements were performed by Thermo ESCALAB 250Xi with monochromatized Al Kα excitation. The calibration was conducted by referring the C1s signal of the contaminate carbon to the binding energy of 284.6 eV. The asymmetric peaks in the XPS spectra were deconvoluted by Lorentzian-Gaussian function. UV-Vis-NIR transmittance spectra were recorded in the range of 200-1200 nm at room temperature by a Varian Cary 5000 spectrophotometer.

High-Resolution Transmission-Electron Microscopy (HRTEM)

Cross-sectional transmission-electron microscopy (TEM) samples were prepared using Focused Ion Beam (FIB) method. TEM imaging and Energy-Dispersive X-ray (EDS) mapping were carried out at 200 kV using Titan ChemiSTEM equipped with a probe Cs corrector and a super-X EDS detector.

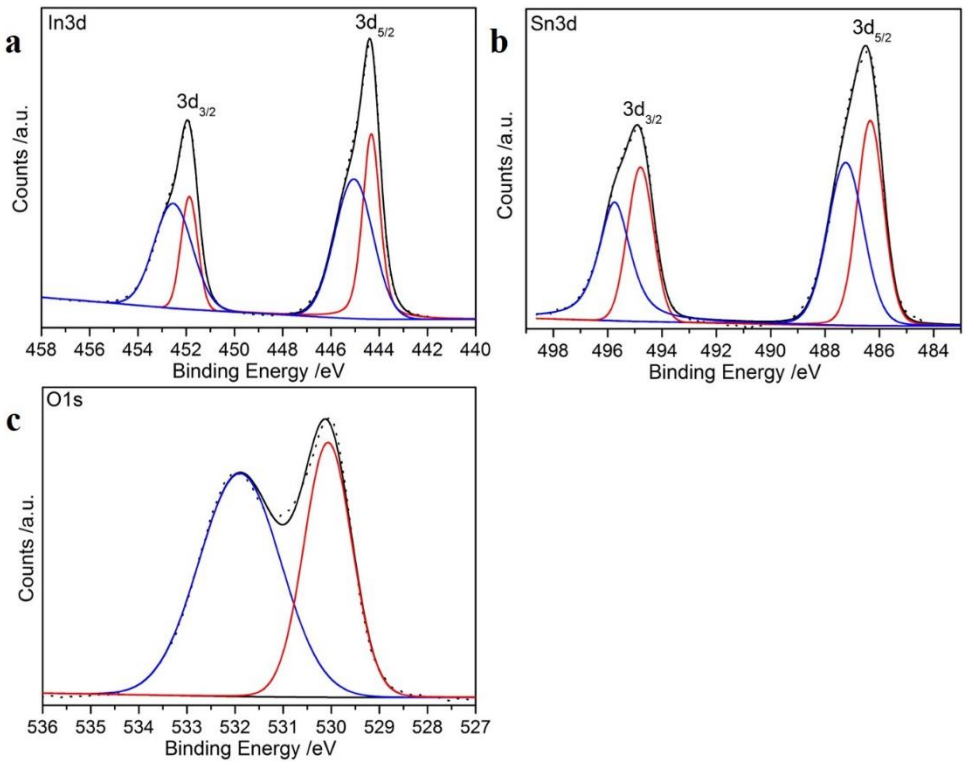

Figure S1 | XPS spectra of the sputtered 10 nm ITO film on the n-Si/TiO_x/ITO photoanode. **a,** In 3d; **b,** Sn 3d and **c,** O 1s. (Dot line: measured results; solid line: fitted results.)

The XPS high resolution peaks and fitted peaks of the In 3d, Sn 3d and O 1s were shown in Fig. S1. The asymmetric peaks have been deconvoluted by Lorentzian-Gaussian function. The In $3d_{5/2}$ Sn $3d_{5/2}$ and O 1s spectra all have been fitted with two peaks. It is noticed that the binding energy of the In $3d_{5/2}$ peak at 444.3 eV, the Sn $3d_{5/2}$ peak at 486.3 eV and the O 1s peak at 530.0 eV for ITO film indicate the formation of crystalline ITO. The binding energy of the In $3d_{5/2}$ (445.0 eV), Sn $3d_{5/2}$ (487.2 eV) and O 1s (531.9 eV) at higher value for ITO film suggest the existence of amorphous ITO.[5] The crystalline and amorphous ITO are co-existed in the 10 nm ITO film.

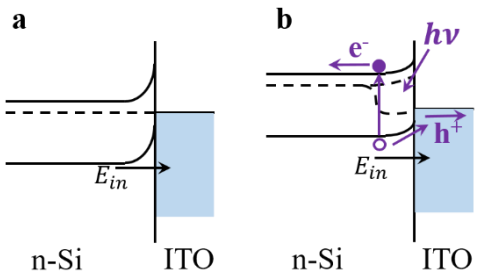

Figure S2 | Schematic illustration of the ideal Schottky structure for n-type silicon with ITO contact. a, Under thermodynamic equilibrium state in the dark. **b,** Under irradiation. (The dash lines represent the Fermi level in the dark, and quasi-Fermi level under illumination. E_{in} represents the built-in electric field. Because of the high conductivity of the ITO, it is assumed that the Fermi level coincides with the conduction band edge in the ITO and the band edges were flat.)

Schottky barrier has been comprehensively utilized in the solar field due to its rectification effect for charge, which is crucial in solar energy conversion.[6,7] It is usually formed between a light absorber (semiconductor) and an outer conduct gate layer (Fig. S2). The work function difference between the composed materials will induce the charge flux near the interface, which then creates an interfacial electric field and Schottky barrier in the semiconductor, eventually resulting in an one-directional current flow under illumination.

Under the ideal cases, the built-in electric field (E_{in}) facile the photoinduced minority carrier in semiconductors to reach the outer conductor layer. The Schottky junction could also be formed with an interposed insulator layer (SiO_2, et. al) between the outer conductor contact and the semiconductor, which is commonly referred as Conductor/Insulator/Semiconductor (CIS) structure. In this type of Schottky junctions, an outer conductor layer with high density of states is required to decrease the charge extraction barrier.[8] For this, the ITO layer is indispensable for the Schottky structure in this article. Without the ITO layer, the holes was hardly to reach the electrode surface, resulted in a poor PEC performance even for ferrocyanide oxidation (Fig. S3). For silicon based devices, there is usually a thin layer of silicon oxide on its surface.[9] In brief, the n-Si/SiO_x/ITO was abbreviated to n-Si/ITO in this article. Based on this, Schottky cells discussed here all possess CIS structures. In general, applied forward bias will decrease the band bending and the barrier height of the junctions, and vice versa.

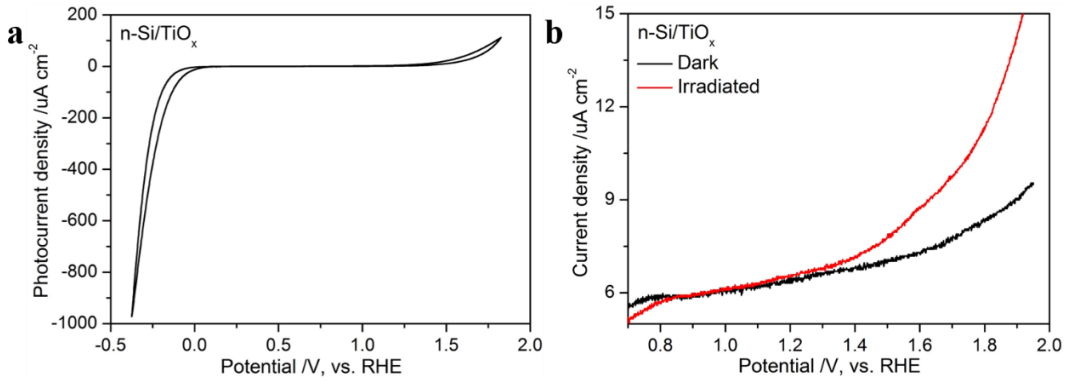

Figure S3 | a, Cyclic Voltammetry curve of the n-Si/TiO_x electrode in ferrocyanide/ ferricyanide solution under 100 mW cm^{-2} AM 1.5G irradiation. **b,** Linear Sweep Voltammetry of the n-Si/TiO_x electrode in 1 M LiOH solution under illumination (red line) and in the dark (black line).

$Fe(CN)_6^{3-/4-}$ is an one-electron, outer-sphere, reversible redox couple. The electrons could be exchanged efficiently between this solution and the electrodes, allowing for evaluating the electronic transport property of the electrodes by cyclic voltammetry scan.[10,11] There is no oxidation or reduction peak appeared in a wide voltage range, indicating a large resistance for charge to reach the n-Si/TiO_x surface (Fig. S3a). Its bad water oxidation performance further confirm the difficulty for charge to get across the TiO_x film without ITO gate layer.

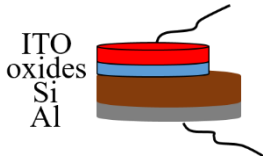

Figure S4 | Schematic illustration of the solid-state cells for the Tafel plots and Capacitance-voltage profiling measurement.

The measurements were carried out on a PARSTAT 2273 work station (Princeton Applied Research). The ITO gate layer acts as the working electrode, the Al layer connects to the counter and the reference electrodes. Scans were taken sweeping from depletion to accumulation with a superimposed 10 mV AC voltage, in order to measure the capacitance. The dark current results from the thermal injection of carriers over a potential barrier. The barrier height is modulated by the amount of the junction voltage. For forward current, electrons are thermally emitted over the potential spike in the conduction band in the ideal n-Si/oxide/ITO structure, and holes are injected into interface states where they recombine with electrons from the ITO.[12]

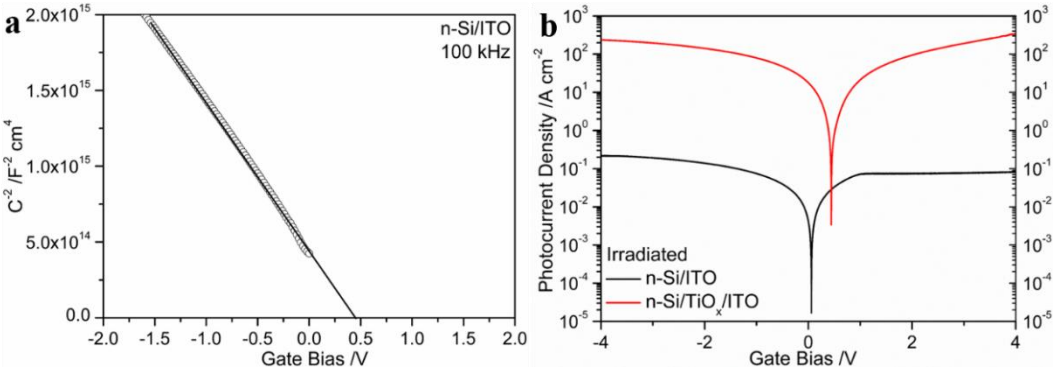

Figure S5 | a, Mott-Schottky plots of the n-Si/ITO Schottky cell measured with the AC potential frequency of 100 kHz in the dark. **b,** Current-Voltage curves of the n-Si/ITO and n-Si/TiO_x/ ITO solid-state cells under illumination

The Mott-Schottky plots were measured with a relatively high AC potential frequency of 100 kHz in order to decrease the influence of the defects and obtain an intrinsic capacitance-voltage response for the calculation of flat band potential. The flat band potential (E_{FB}) calculated from the intercept of the linear fitted line on the horizontal axis is about 0.45 eV. Combining with the difference in energy between the Fermi level and the conduction band of n-Si ($V_n = 0.17\ eV$) mentioned in the material and methods section, then the barrier height of the n-Si/ITO Schottky cell can be calculated as $\Phi_b = E_{FB} + V_n = 0.62\ eV$.

The photocurrent density is due to the generation and collection of light-induced carriers. The incident light and the gate area of the n-Si/ITO is almost the same as that of the n-Si/TiO_x/ITO cell, but the photocurrent density obtained with the former is far less than that with the latter (Fig. S5b). Then, the most critical parameter, which influence the photocurrent density, is the diffusion length and the minority carrier lifetime. Here, the photo-induced carriers of n-Si/ITO cell seems to behave a shorter diffusion length or lifetime.

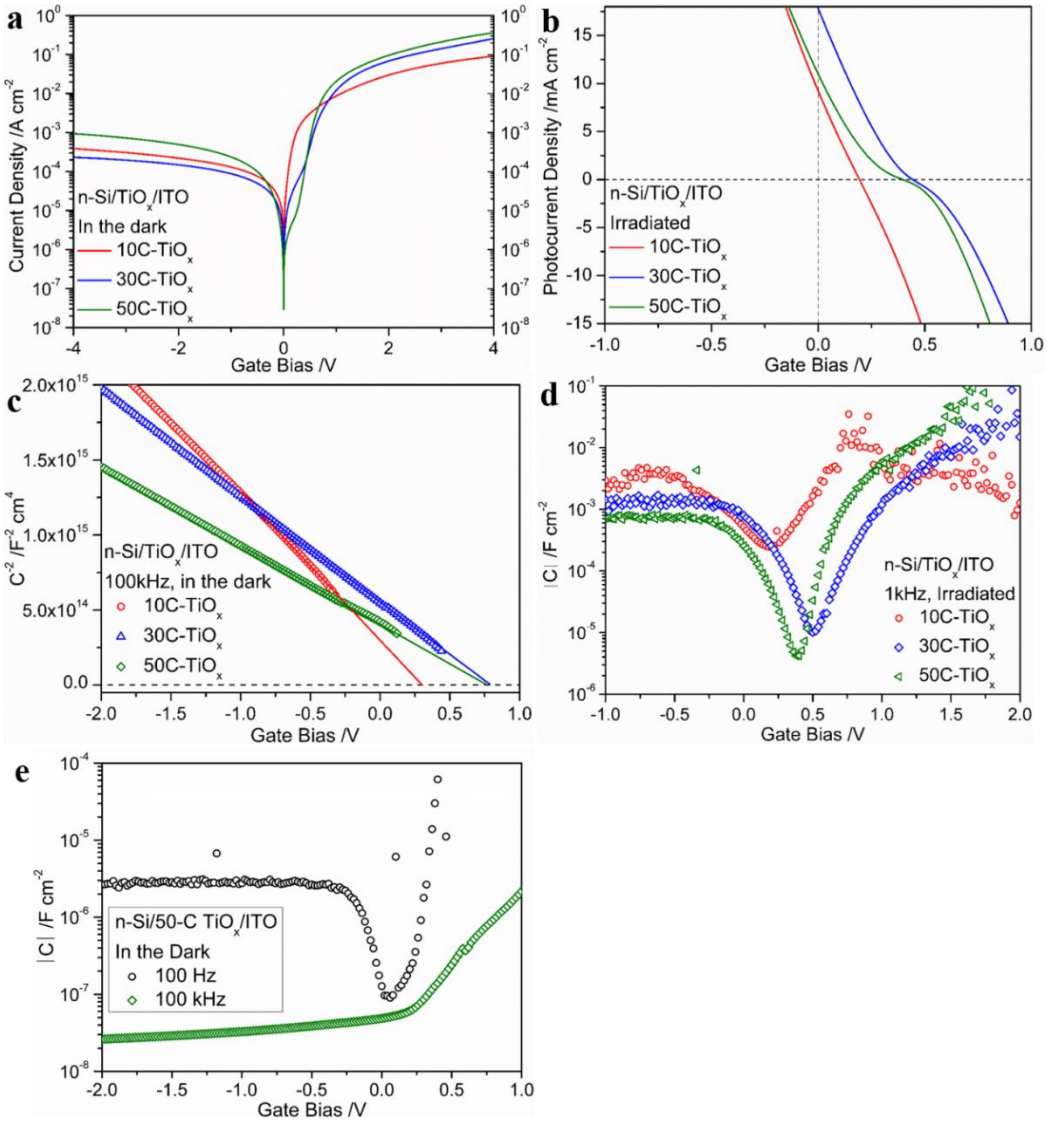

Figure S6 | a, b, The Current-Voltage curves **c,** Mott-Schottky plots and **d,** Capacitance-Voltage profiling of the n-Si/TiO_x/ITO solid cells with different TiO_x thickness under illumination or in the dark. **e,** Capacitance-Voltage profiling of the n-Si/50C-TiO_x/ITO solid cell tested with different AC frequency in the dark.

Table S1 | The V_{oc}, J_{sc} and E_{FB} of the n-Si/TiO_x/ITO cells mentioned in Fig. S6.

n-Si/TiO_x/ITO	V_{oc}	J_{sc}	E_{FB}
10C-TiO_x	0.19 V	9.1 mA cm^{-2}	0.3 V
30C-TiO_x	0.45 V	17.8 mA cm^{-2}	0.78 V
50C-TiO_x	0.39 V	10.8 mA cm^{-2}	0.76 V

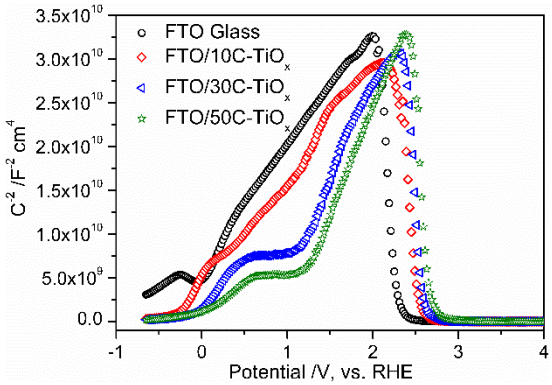

Figure S7 | Mott-Schottky plots of blank FTO glass and FTO/TiO_x films were carried out in 1 M LiOH solution (pH=12) with the AC potential frequency of 1 kHz in the dark. It was used to analyze the intraband electric states of the TiO_x.

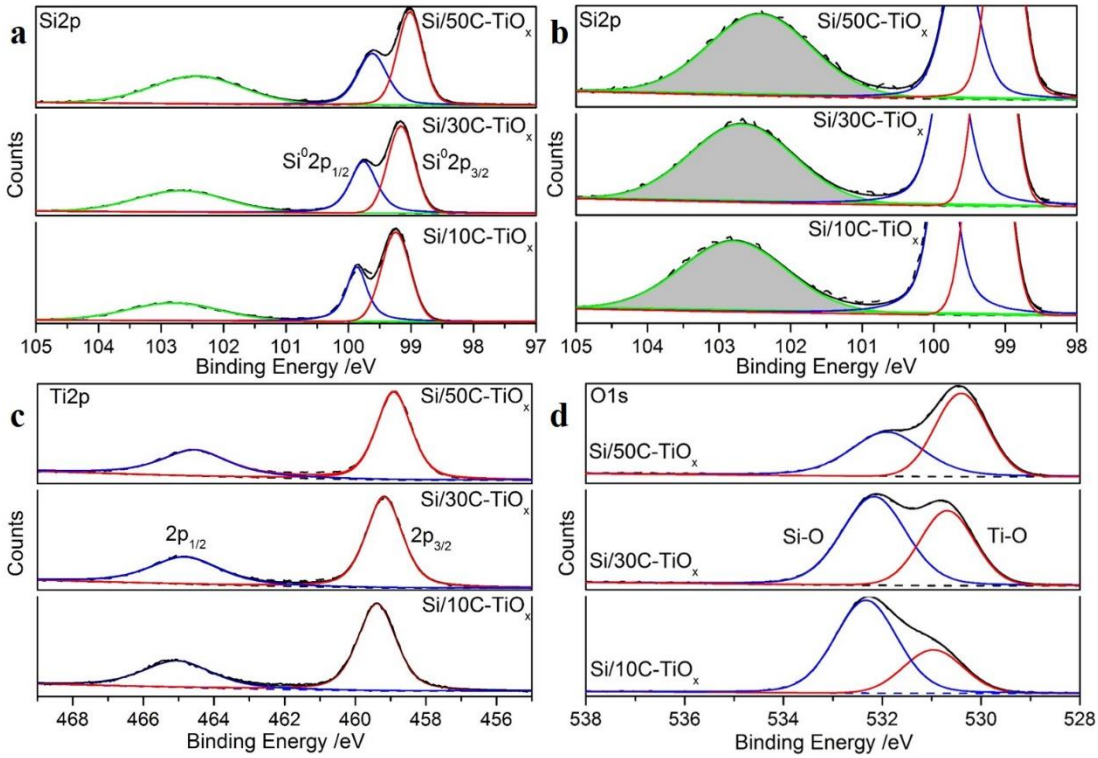

Figure S8 | XPS spectra of n-Si/TiO_x with different TiO_x coverages **a,** Si 2p. **b,** Enlarged Si 2p. **c,** Ti 2p. **d,** O 1s. (Dash line: measured results; solid line: fitted results.)

Table S2 | Binding Energies for Si 2p, Ti 2p and O 1s Fitted Peaks in Figure S8

	Si^0 $2p_{3/2}$	Si^0 $2p_{1/2}$	$Si^{2+\sim3+}$ 2p	Ti $2p_{3/2}$	Ti $2p_{1/2}$	O 1s Ti-O	O 1s Si-O
Si/10C-TiO_x	99.3 eV	99.9 eV	102.8 eV	459.4 eV	465.0 eV	531.0 eV	532.3 eV
Si/30C-TiO_x	99.2 eV	99.8 eV	102.7 eV	459.2 eV	464.8 eV	530.7 eV	532.2 eV
Si/50C-TiO_x	99.0 eV	99.6 eV	102.4 eV	458.9 eV	464.6 eV	530.4 eV	532.0 eV

To further prove the changes of the interfacial species along with the introduction of TiO_x, the XPS spectra are employed to identify the variation at the solid-solid interface. TiO_x with different thickness were loaded on the HF treated n-Si (100) wafers for XPS characterization. Fig. S8 shows the XPS spectra of the Si 2p, Ti 2p and O 1s. The binding energy (BE) of C 1s (284.6 eV) was taken as a reference to correct the binding energy of the samples. The asymmetric peak in Fig. S6a can be well fitted by two components at around 99.6 and 99.0 eV, which corresponds to the Si $2p_{1/2}$ and Si $2p_{3/2}$ of the silicon (Si^0), respectively.[13] And the broad peaks near 102 eV can be

assigned to reacted Si, which is present in various oxidation states such as Si^{2+} and Si^{3+} deriving from interfacial reactions between the surface Si species and the TiO_x overlayer (Fig. S8b).[14] The Si-O-Ti interfacial species may be formed during the interfacial reactions.[15] The doublet peaks at 464.6 and 459.0 eV can be described as the Ti $2p_{1/2}$ and Ti $2p_{3/2}$ with a spin-orbit splitting of 5.6 eV (Fig. S8c).[16] The spectra of the O 1s region is shown in Fig. S8d, the O 1s peaks can also be well fitted by two components near 530.7 and 532.2 eV. The peak centered at the lower BE value is designated as O-Ti, and the other one is assigned to O-Si species.[15] BE of the $Ti2p_{3/2}$ peak at 458.9 eV and the O1s peak at 530.4 eV for 50C-TiO_x indicate the formation of bulk TiO_2.[17] The BE values of the $Ti2p_{3/2}$ shift to the higher energy for samples with thinner TiO_x (10C and 30C). This shift can be attributed to the low TiO_x coverages, where the TiO_x-support interaction is higher, the BE is higher than those of bulk TiO_2.[18] The XPS data clearly illustrated the strong interaction between surface Si species and TiO_x overlayer, which may modify the interface properties.

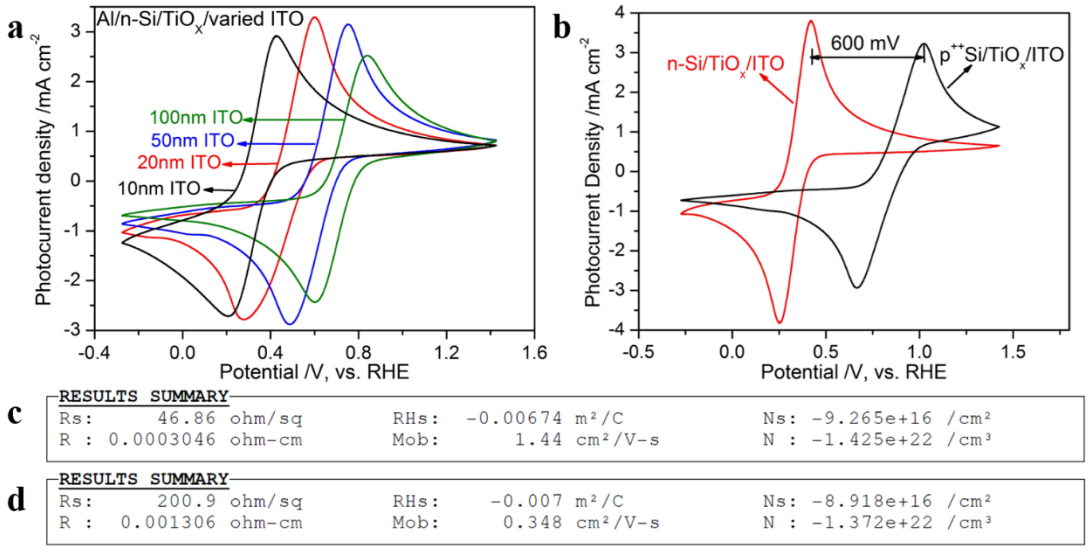

Figure S9 | a, Cyclic voltammetry curves of n-Si/TiO_x/ITO photoanodes with varied ITO thickness tested in 10 mM ferri/ferrocyanide solution under AM 1.5 G irradiated. **b,** Cyclic voltammetry curves of n-Si/TiO_x/ITO (irradiated) and p^{++}-Si/TiO_x/ITO (in the dark) electrodes with 10 nm ITO layer tested in 10 mM ferri/ferrocyanide solution. **c –d,** Hall Effect Measurements for the sputtered ITO layers with different thickness, 65 nm and 197 nm respectively.

As shown in Fig. S9a, the oxidation peaks for $Fe(CN)_6^{4-}$ oxidation shift positively along with the increased thickness of TiO_x films, indicating a decreased photovoltage. This is due to the increased holes transfer resistance caused by ITO layer. As shown in Fig. S9c-d, the resistance of the ITO films is enhanced with increasing its thickness.

The photovoltaic response of p^{++}-Si/TiO_x/ITO electrodes is almost the same as that in the dark due to the high doping concentration of p^{++}-Si. The p^{++}-Si has a high density of holes both in the dark and under illumination, but the concentration change of the photoinduced electrons is very small due to its high doping level. It is usually used to illustrate the PEC performance of the silicon based anode in the dark (Fig. S9b).

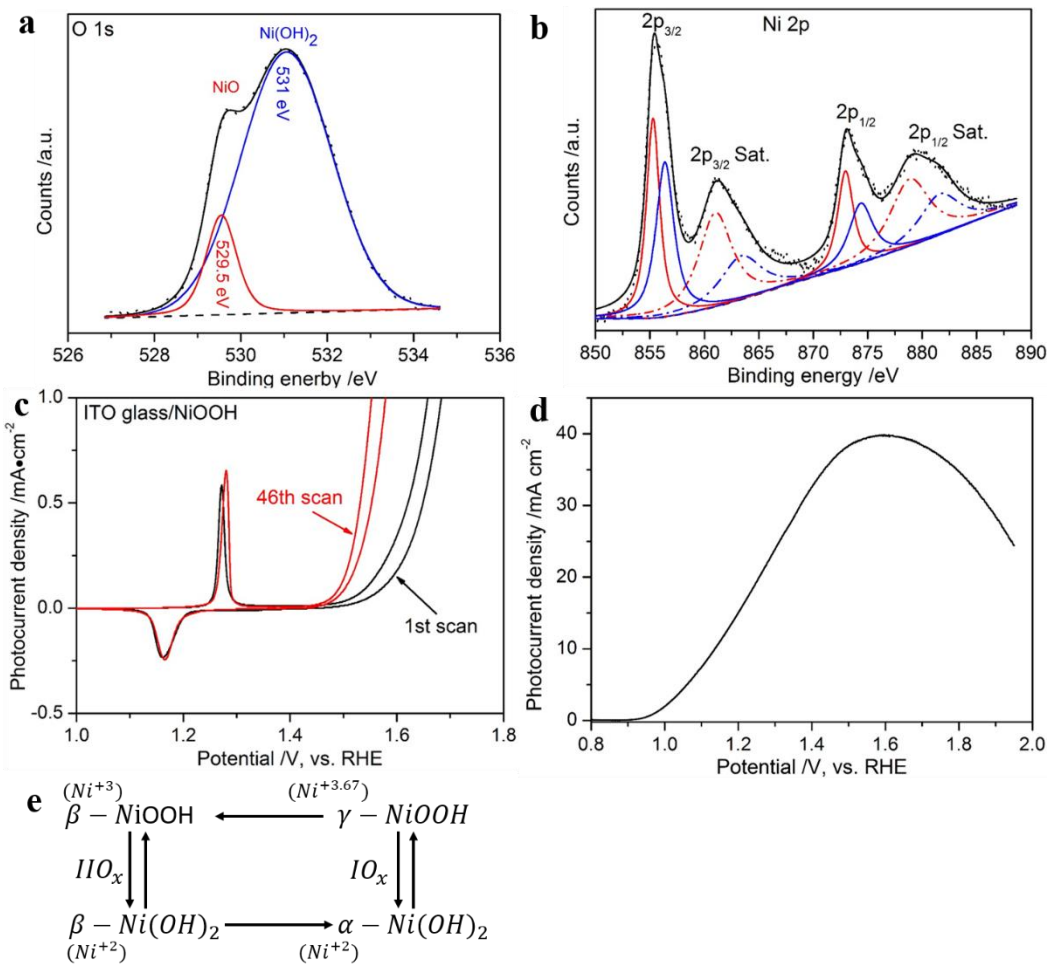

Figure S10 | XPS spectra of PEC deposited nickel compounds **a,** O1s and **b,** Ni 2p. (Dot line: measured results; solid line, dash and dash dot line: fitted results.) **c,** Cyclic Voltammogram curves of ITO glass/NiOOH electrode for the first scan (black line) and the 46th scan (red line) in 1 M LiOH solution. **d,** The difference value between the photocurrent density of n-Si/TiO_x/ITO/NiOOH and the current density of p^{++}-Si/TiO_x/ITO/NiOOH. e, The Ni(II)/Ni(III) redox transitions in Ni hydroxide layers.[19]

Table S3 | Binding Energies for O 1s and Ni 2p Fitted Peaks in Figure S10

O1s	Ni $2p_{3/2}$	Ni $2p_{3/2\ sat.}$	Ni $2p_{1/2}$	Ni $2p_{1/2\ sat.}$
529.5 eV [a]	855.3 eV [d]	861.0 eV [d]	873.0 eV [d]	878.8 eV [d]
530.7 eV [b]	856.4 eV [e]	863.4 eV [e]	874.4 eV [e]	881.6 eV [e]
531.7 eV [c]				

[a]O 1s for NiO. [b]O 1s for $Ni(OH)_2$. [c]O 1s for NiOOH. [d]Ni 2p for NiO/$Ni(OH)_2$. [e]Ni 2p for NiOOH.

The nickel oxide hydroxide (NiOOH) was loaded on the n-Si/TiO_x/ITO electrode through photoelectrochemical deposition method. The asymmetry O 1s and Ni 2p XPS peaks were fitted into several peaks (Fig. S10), the fitted results were listed in Table S3. The analysis results of the O1s and Ni2p spectra have verified the co-existence of NiO, $Ni(OH)_2$ and NiOOH in the film.[20,21] The film of nickel oxide is going through a transition between NiO/$Ni(OH)_2$ to NiO/NiOOH during water oxidation in alkali solution.[22] A redox peaks at around 1.1~1.3 V (vs. RHE) can be observed from the Cyclic Voltammetry curves of the deposited Ni compound (Fig. S10c). The electrochemical redox reactions of the film are primarily dominated by the OH^- ion insertion/ extraction reactions.[23] The involved electrochemical redox reactions can be given as $Ni(OH)_2 + OH^- \leftrightarrow NiOOH + H_2O + e^-$ and $NiO + OH^- \leftrightarrow NiOOH + e^-$. The redox potential of $Ni(OH)_2$/NiOOH depends on the inter-sheet distance and charge capacity of $Ni(OH)_2$/NiOOH. The inter-sheet distance and charge capacity of the α-$Ni(OH)_2$/γ-NiOOH is larger than that of β-$Ni(OH)_2$/β-NiOOH, so a smaller redox potential can be expected for the former transition.[24] The redox reaction is showed as a couple of cathodic and anodic current peaks emerged in the applied potential range of 0.212-0.216 V and 0.322-0.330 V (vs. SCE), respectively (Fig. S10c). The position of the redox peaks shifts slightly along with the increasing number of scans. The standard electrode potential of the electrochemical redox reaction of the NiOOH is calculated to be ~1.22 V (vs. RHE), which can be assigned to the transition of α-$Ni(OH)_2$/γ-NiOOH. The β-$Ni(OH)_2$/β-NiOOH will presents a higher redox potential.[25] So, there is mainly γ-NiOOH existed in our deposited film.

Because that the positive charge is the major carrier in the p^{++}-Si, irradiation has little impact on the total concentration of holes in the semiconductor. So, there is no difference between the current density of p^{++}-Si/TiO_x/ITO/NiOOH measured under irradiation and in the dark.

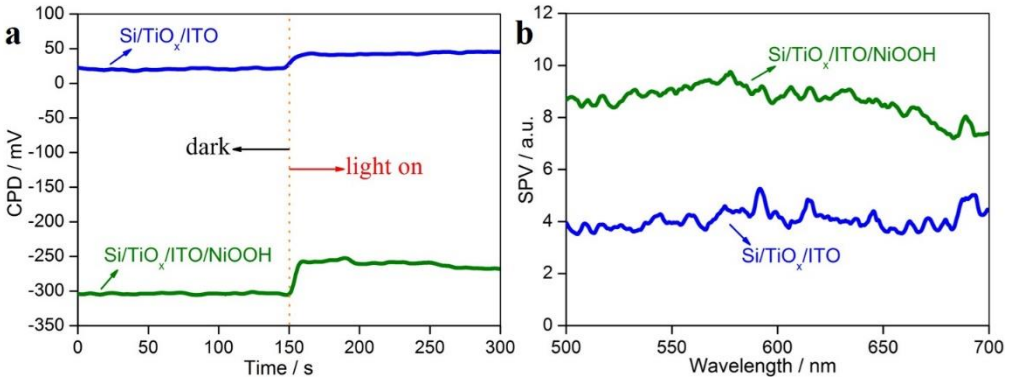

Figure S11 | a, Surface potential difference (CPD) and **b,** Steady-state surface photovoltage (SPV) spectroscopy of the n-Si/TiO_x/ITO and n-Si/TiO_x/ITO/NiOOH photoanodes measured under solution free conditions in air.

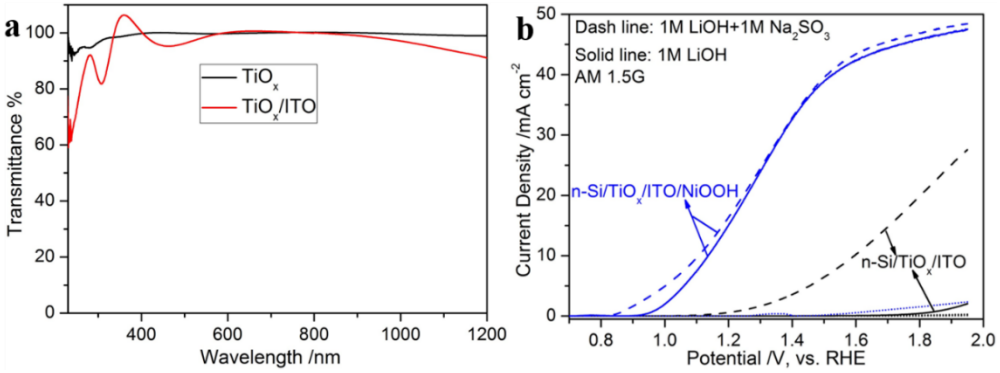

Figure S12 | a, Transmission spectra of the TiO_x and TiO_x/ITO films. **b,** Linear Sweep Voltammetry curves of n-Si/TiO_x/ITO (black) and n-Si/TiO_x/ITO/NiOOH (blue) in 1 M LiOH (solid line) and 1 M LiOH with 1 M Na_2SO_3 solution (dash line) under 100 mW cm $^{-2}$ AM 1.5G irradiation at a 20 mV s^{-1} scan rate. Dot lines: in the dark.

Hole scavenger sodium sulfite (1M Na_2SO_3) was introduced to examine the photoelectrochemical properties of the electrodes. The oxidation of sulfite is thermodynamically and kinetically more facile than oxidation of water, therefore, measuring photocurrent for sulfite oxidation enables investigation of the PEC properties of photoanode independently of the water oxidation kinetics.[1] The typical photocurrent-potential (J-V) curves of the sulfite oxidation and water oxidation with n-Si/TiO_x/ITO and n-Si/TiO_x/ITO/NiOOH are shown in Fig. S12. Photocurrent density obtained for sulfite oxidation was used to calculate charge injection efficiency ϕ_{inj} and charge separation efficiency ϕ_{sep} using the method listed in the equation S1, the results were presented in Fig.9b.

$$J = J_{abs} * \Phi_{sep} * \Phi_{inj} \qquad \text{Equation S1-1}$$

$$\Phi_{inj} = \frac{J_{H_2O}}{J_{Na_2SO_3}} \qquad \text{Equation S1-2}$$

$$\Phi_{sep} = \frac{J_{Na_2SO_3}}{J_{abs}} \qquad \text{Equation S1-3}$$

Φ_{inj} is assumed to be 1 for the sulfite oxidation. The separation efficiency was calculated according to the assumed hypersorption of incident light (J_{abs}=43.7 mA cm^{-2}).

Table S4 | PEC performance of the reported silicon photoanodes

Photoanode	Onset potential (V, vs. RHE)	Current density at 1.23 V(mA cm^{-2})	Saturated Current density (mA cm^{-2})
n-Si/SiO_x/TiO_x/Ir [11]	1.03 in NaOH	8.89	Null
	0.95 in H_2SO_4	14.72	Null
np^+-Si/Co/CoPi [26]	0.85	1.70	Null
npp^+-Si/ITO/CoPi [27]	1.09	1.22	Null
n-Si/NiO_x [28]	1.10	0.24	Null
npp^+-Si/FTO/CoBi [29]	1.09	2.73	Null
n-Si/SiO_x/Ni/NiO_x [30]	1.05	11.76	54.7 (2 Sun)
np^+-Si/TiO_x/Ni [10]	1.11	12	35.9
np^+-Si/CoO_x [31]	1	14.57	29.6
np^+-Si/Ni/Fe:NiO_x [32]	1.05	< 19.69	19.7
np^+-Si/Ir/IrO_x [33]	1	14.35	Null
n-Si/Ferroelectric layer/Ni [34]	1.07	12.43	24.6
n-Si/TiO_x/Ni [35]	1.2	1	28.5
n-Si/SiO_x/Co/CoOOH [36]	1.1	13.12	35.6
np^+-Si/TiO_x/$NiCrO_x$ [37]	1.07	3.6	6.5
np^+-Si/$NiCo_2O_4$/NiFe [38]	1	24	30.8
np^+-Si/NiO_x [39]	1	29	34.9
n-Si/NiO_x [39]	1.25	Null	30.7
HTJ-Si cells/ITO/NiO_x [40]	0.95	25	35.4
n-Si/SiO_x/CoO_x/NiO_x [41]	0.98	28	30.8
n-Si/SiO_x/Cu/CuO [42]	1.28	Null	Null
np^+-Si/SiO_x/Ti/Ni [43]	0.96	27	28.2
n-Si/SiO_x/TiO_x/ITO/NiOOH (This work)	0.9	18	40

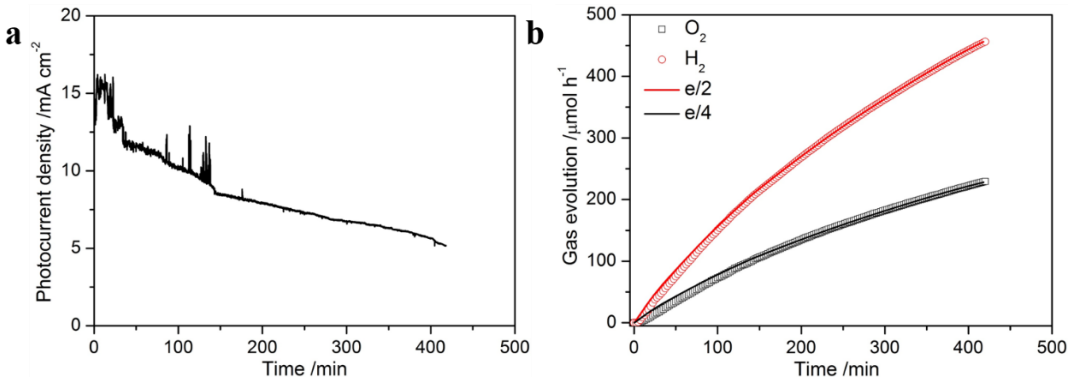

Figure S13 | a, I-t curves of the n-Si/TiO_x/ITO/NiOOH photoanode under 300 W Xenon lamp irradiation in 1 M LiOH solution with an applied voltage of 0.28 V (vs. SCE). **b,** Corresponding gas evolution, e/2 and e/4 amounts of the n-Si/TiO_x/ITO/NiOOH photoanode.

Gas evolution was carried out in a three-electrode cell connected to a closed gas circulation and evacuation system. Pt foil acted as the counter electrode and the SCE was used as the reference electrode. The n-Si/TiO_x/ITO/NiOOH photoanode was used as the working electrode. The counter electrode and the working electrode with the reference electrode were dipped in 100 mL 1M LiOH electrolyte and separated by a proton exchange membrane. The system was thoroughly degassed and then irradiated by a 300 W Xenon lamp. An external voltage of 0.28 V (vs. SCE) was applied on the working electrode. Evolved O_2 and H_2 were analyzed by an online gas chromatograph with thermal conductivity detector (Agilent GC 7890, 5A zeolite column and Ar carrier).

As shown in Fig. S13, even though the photocurrent density declined to some extent after long term operation, the Faradic efficiency of the photoanode is almost 100%, indicating that the Si substrate is relatively stable under long term operation. Because if the silicon was corroded a lot in alkaline solution, the generated H_2 from the corrosion reaction will eventually make the Faradic efficiency deviate from 100%. Then, the instability of the photoanode was mainly related to the property of NiOOH.

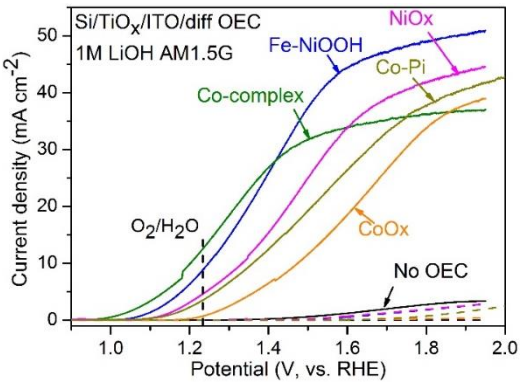

Figure S14 | Linear Sweep Voltammetry curves of n-Si/TiO_x/ITO with different oxygen evolution catalysts under 100 mW cm^{-2} AM 1.5G irradiation at a 20 mV s^{-1} scan rate. Dash lines: in the dark.

A thin layer (about 2 nm) of metallic Ni or Co was deposited on the surface of n-Si/TiO_x/ITO through D. C. sputtering method. The NiO_x and CoO_x were formed during PEC testing through the in-situ oxidation of metal films. The Co-Pi and Fe doped NiOOH were prepared through PEC deposition method. The Co-complex is a molecular catalyst, which is deposited through direct dipping and drying. All samples were tested in 1M LiOH solution except the one with Co-Pi and Co-complex. Samples with Co-Pi and Co-complex were tested in neutral phosphate buffer (pH=6.8).

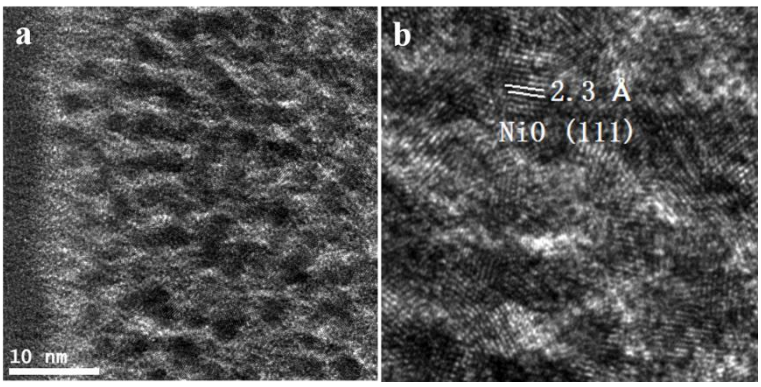

Figure S15 | a, HRTEM image and **b,** the corresponding enlarged HRTEM image of the NiOOH layer.

References

(1) Kim, T. W.; K Choi, Y. S. *Science* **2014**, *343*, 990.

(2) Melitz, W.; Shen, J.; Kummel, A. C.; Lee, S. *Surf. Sci. Rep.* **2011**, *66*, 1.

(3) Kronik, L.; Shapira, Y. *Surf. Sci. Rep.* **1999**, *37*, 1.

(4) Zhu, J.; Fan, F.; Chen, R.; An, H.; Feng, Z.; Li, C. *Angew. Chem., Int. Ed.* **2015**, *54*, 9111.

(5) Thogersen, A.; Rein, M.; Monakhov, E.; Mayandi, J.; Diplas, S. *J. Appl. Phys.* **2011**, *109*, 113532.

(6) Yan, K.; Wei, Z.; Li, J.; Chen, H.; Yi, Y.; Zheng, X.; Long, X.; Wang, Z.; Wang, J.; Xu, J.; Yang, S. *Small* **2015**, *11*, 2269.

(7) Bai, S.; Li, X.; Kong, Q.; Long, R.; Wang, C.; Jiang, J.; Xiong, Y. *Adv. Mater.* **2015**, *27*, 3444.

(8) Scheuermann, A. G.; Lawrence, J. P.; Kemp, K. W.; Ito, T.; Walsh, A.; Chidsey, C. E.; Hurley, P. K.; McIntyre, P. C. *Nat. Mater.* **2015**, *15*, 99.

(9) Scheuermann, A. G.; Prange, J. D.; Gunji, M.; Chidsey, C. E. D.; McIntyre, P. C. *Energy Environ. Sci.* **2013**, *6*, 2487.

(10) Hu, S.; Shaner, M. R.; Beardslee, J. A.; Lichterman, M.; Brunschwig, B. S.; Lewis, N. S. *Science* **2014**, *344*, 1005.

(11) Chen, Y. W.; Prange, J. D.; Duhnen, S.; Park, Y.; Gunji, M.; Chidsey, C. E. D.; McIntyre, P. C. *Nat. Mater.* **2011**, *10*, 539.

(12) Thompson, W. G.; Anderson, R. L. *Solid-state Electron.* **1978**, *21*, 603.

(13) Godet, C.; Fadjie-Djomkam, A. B.; Ababou-Girard, S.; Tricot, S.; Turban, P.; Li, Y.; Pujari, S. P.; Scheres, L.; Zuilhof, H.; Fabre, B. *J. Phys. Chem. C* **2014**, *118*, 6773.

(14) Cho, Y. S.; Heo, J. S.; Kim, J. C.; Moon, S. H. *Chem. Vap. Deposition* **2006**, *12*, 659.

(15) Sasahara, A.; Pang, C. L.; Tomitori, M. *J. Phys. Chem. C* **2010**, *114*, 20189.

(16) So1dergren, S.; Siegbahn, H. *J. Phys. Chem. B* **1997**, *101*, 3087.

(17) Dementjev, A. P. *J. Vac. Sci. Technol., A* **1994**, *12*, 423.

(18) Lassaletta, G.; Caballero, A.; Wu, S.; Gonzhlez-Elipe, A. R.; Fernhdez, A. *Vacuum* **1994**, *45*, 1085.

(19) Malara, F.; Minguzzi, A.; Marelli, M.; Morandi, S.; Psaro, R.; Dal Santo, V.; Naldoni, A. *ACS Catalysis* **2015**, *5*, 5292.

(20) Mansour, A. N. *Surf. Sci. Spectra* **1994**, *3*, 271.

(21) Ratcliff, E. L.; Meyer, J.; Steirer, K. X.; Garcia, A.; Berry, J. J.; Ginley, D. S.; Olson, D. C.; Kahn, A.; Armstrong, N. R. *Chem. Mater.* **2011**, *23*, 4988.

(22) Hoppe, H.-W.; Strehblow, H.-H. *Surf. Interface Anal.* **1989**, *14*, 121.

(23) Gao, T.; Jelle, B. P. *J. Phys. Chem. C* **2013**, *117*, 17294.

(24) Huang, J. J.; Hwang, W. S.; Weng, Y. C.; Chou, T. C. *Mater. Trans.* **2010**, *51*, 2294.

(25) Oliva, P.; Leonardi, J.; Laurent, J. F. *J. Power Sources* **1982**, *8*, 229.

(26) Young, E. R.; Costi, R.; Paydavosi, S.; Nocera, D. G.; Bulović, V. *Energy Environ. Sci.* **2011**, *4*, 2058.

(27) Pijpers, J. J. H.; Winkler, M. T.; Surendranath, Y.; Buonassisi, T.; Nocera, D. G. *Proc. Natl. Acad. Sci.* **2011**, *108*, 10056.

(28) Sun, K.; Park, N.; Sun, Z.; Zhou, J.; Wang, J.; Pang, X.; Shen, S.; Noh, S. Y.; Jing, Y.; Jin, S.; Yu, P. K. L.; Wang, D. *Energy Environ. Sci.* **2012**, *5*, 7872.

(29) Cox, C. R.; Winkler, M. T.; Pijpers, J. J. H.; Buonassisi, T.; Nocera, D. G. *Energy Environ. Sci.* **2013**, *6*, 532.

(30) Kenney, M. J.; Gong, M.; Li, Y.; Wu, J. Z.; Feng, J.; Lanza, M.; Dai, H. *Science* **2013**, *342*, 836.

(31) Yang, J. H.; Walczak, K.; Anzenberg, E.; Toma, F. M.; Yuan, G. B.; Beeman, J.; Schwartzberg, A.; Lin, Y. J.; Hettick, M.; Javey, A.; Ager, J. W.; Yano, J.; Frei, H.; Sharp, I. D. *J. Am. Chem. Soc.* **2014**, *136*, 6191.

(32) Mei, B.; Permyakova, A. A.; Frydendal, R.; Bae, D.; Pedersen, T.; Malacrida, P.; Hansen, O.; Stephens, I. E.; Vesborg, P. C.; Seger, B.; Chorkendorff, I. *J. Phys. Chem. Lett.* **2014**, *5*, 3456.

(33) Mei, B.; Seger, B.; Pedersen, T.; Malizia, M.; Hansen, O.; Chorkendorff, I.; Vesborg, P. C. *J. Phys. Chem. Lett.* **2014**, *5*, 1948.

(34) Cui, W.; Xia, Z.; Wu, S.; Chen, F.; Li, Y.; Sun, B. *ACS Appl. Mater. Interfaces* **2015**, *7*, 25601.

(35) McDowell, M. T.; Lichterman, M. F.; Carim, A. I.; Liu, R.; Hu, S.; Brunschwig, B. S.; Lewis, N. S. *ACS Appl. Mater. Interfaces* **2015**, *7*, 15189.

(36) Hill, J. C.; Landers, A. T.; Switzer, J. A. *Chem. Mater.* **2015**, *14*, 1150.

(37) Shaner, M. R.; Hu, S.; Sun, K.; Lewis, N. S. *Energy Environ. Sci.* **2015**, *8*, 203.

(38) Chen, L.; Yang, J.; Klaus, S.; Lee, L. J.; Woods-Robinson, R.; Ma, J.; Lum, Y.; Cooper, J. K.; Toma, F. M.; Wang, L. W.; Sharp, I. D.; Bell, A. T.; Ager, J. W. *J. Am. Chem. Soc.* **2015**, *137*, 9595.

(39) Sun, K.; McDowell, M. T.; Nielander, A. C.; Hu, S.; Shaner, M. R.; Yang, F.; Brunschwig, B. S.; Lewis, N. S. *J. Phys. Chem. Lett.* **2015**, *6*, 592.

(40) Sun, K.; Saadi, F. H.; Lichterman, M. F.; Hale, W. G.; Wang, H. P.; Zhou, X. H.; Plymale, N. T.; Omelchenko, S. T.; He, J. H.; Papadantonakis, K. M.; Brunschwig, B. S.; Lewis, N. S. *Proc. Natl. Acad. Sci.* **2015**, *112*, 3612.

(41) Zhou, X.; Liu, R.; Sun, K.; Friedrich, D.; McDowell, M. T.; Yang, F.; Omelchenko, S. T.; Saadi, F. H.; Nielander, A. C.; Yalamanchili, S.; Papadantonakis, K. M.; Brunschwig, B. S.; Lewis, N. S. *Energy Environ. Sci.* **2015**, *8*, 2644.

(42) Shi, Y.; Gimbert-Surinach, C.; Han, T.; Berardi, S.; Lanza, M.; Llobet, A. *ACS Appl. Mater. Interfaces* **2016**, *8*, 696.

(44) Oh, S.; Oh, J. *J. Phys. Chem. C* **2016**, *120*, 133.